19 Interferometry-Based Optoacoustic Tomography

Hagyong Kihm
Space Optics Research Center

Stefan A. Carp
Harvard Medical School

Vasan Venugopalan
University of California

CONTENTS

19.1 Introduction 239
19.2 Overview of Optoacoustics and Interferometry 239
19.3 Optoacoustics Using Homodyne Interferometry 241
19.4 Optoacoustic Tomography Using Heterodyne Interferometry 242
19.4.1 Experimental Setup 243
19.4.2 Image Reconstruction Algorithm 244
19.4.3 Tissue Phantom Results 245
19.4.4 Animal Model Results 246
19.5 Optoacoustics Using Confocal Fabry-Perot Interferometry 247
19.6 Conclusions and Future Directions 247
References 248

19.1 INTRODUCTION

The use of optical methods to measure stress waves has been pursued as an alternative to piezoelectric transducers for over 40 years [1–3]. While a variety of optical approaches using knife-edge, beam deflection, and diffraction have been developed [2,4], interferometric methods now seem to predominate. Optical methods have several attractive characteristics that differentiate their usage from conventional piezoelectric transducers. Specifically, optical methods do not require acoustic contact between target and sensor [5], and provide for simple strategies to measure stress waves at locations coincident with the delivery of laser radiation. Moreover, optical techniques generally have better bandwidth characteristics and require no calibration [6]. In fact, the use of laser interferometry for the calibration of hydrophones has already become standard practice [7]. Optical approaches, when used in conjunction with imaging optics, also allow measurement over a broad area with high spatial resolution [8,9]. These benefits notwithstanding, the robust use of interferometric methods for optoacoustic imaging requires careful design and implementation to minimize difficulties associated with alignment and long-term stability for biomedical application.

A proper understanding of optical interferometry is essential for its proper application to measure the thermoelastic stress and displacement fields generated by pulsed laser radiation. Following this introduction, we begin in Section 19.2 with a brief exposition of the physical principles underlying thermoelastic stress and displacement generation, and how these thermoelastic effects can be measured using interferometry. This overview is followed by individual sections detailing the use of homodyne (Section 19.3), heterodyne (Section 19.4), and confocal Fabry-Perot (Section 19.5) interferometry in optoacoustics. In each section, we provide examples of the use of these interferometric techniques for optoacoustic imaging and discuss their strengths and limitations relative to other approaches. We conclude in Section 19.6 by articulating the challenges and future directions for interferometric optoacoustic imaging.

19.2 OVERVIEW OF OPTOACOUSTICS AND INTERFEROMETRY

Optoacoustics refers to the generation of acoustic/stress waves via optical excitation. The underlying mechanism for

this stress generation is the temperature rise that results from optical absorption, resulting in thermal expansion with associated propagation of both stress and displacement waves. For a laser pulse duration t_p, both time-resolved stress and displacement fields measured at the target surface contain sufficient information to resolve objects with size on the order of $\delta \gtrsim v_s t_p$, where v_s is the speed of longitudinal stress wave propagation in the medium. Thus, one can measure either the thermoelastic stresses or the associated displacements with suitable sensors, and image the spatial distribution of the absorbed energy density within the object using appropriate reconstruction algorithms. This reconstruction provides a subsurface imaging modality that is referred to as optoacoustic tomography [10].

The time-resolved measurement of thermoelastic stress waves is most often accomplished using piezoelectric transducers composed of ceramic materials or polymers, such as polyvinylidene difluoride (PVDF). This approach requires acoustic contact between the piezoelectric sensor and the sample to be imaged. The temporal profile of the measured stress is related to the spatial distribution of the laser-induced temperature rise in the target [11,12]. Optical interferometry, on the other hand, can be used to measure the surface displacement associated with the thermoelastic response of the target [13]. Within the theory of linear elasticity, the thermoelastic wave equation for the displacement vector $\mathbf{u}(\mathbf{r},t)$ is given by [14,15]:

$$\rho \frac{\partial^2 \mathbf{u}}{\partial t^2} - \frac{E}{2(1+\nu)}\nabla^2 \mathbf{u} - \frac{E}{2(1+\nu)(1-2\nu)}\nabla(\nabla \cdot \mathbf{u}) = \frac{-E\beta}{3(1-2\nu)}\nabla T, \tag{19.1}$$

where E is Young's modulus, ν is Poisson's ratio, β is the coefficient of thermal expansion, and $T(\mathbf{r},t)$ is the temperature rise. Numerical solution of this three-dimensional wave equation provides the relationship between the spatial distribution of the temperature rise (and thus the absorbed energy density) and the displacement [16,17]. The relationship between the stress tensor and the displacement is provided by the stress-strain $(\sigma - \varepsilon)$ and strain-displacement $(\varepsilon - u)$ relationships for a linearly elastic solid as follows:

$$\sigma_{ik} = \frac{E}{1+\nu}\left(\varepsilon_{ik} + \frac{\nu}{1-2\nu}\varepsilon_{jj}\delta_{ik}\right) - \frac{E\beta T}{3(1-2\nu)}\delta_{ik}, \tag{19.2}$$

$$\varepsilon_{ij} = \frac{1}{2}\left(u_{i,j} + u_{j,i}\right). \tag{19.3}$$

When a target is probed by interferometry, the surface displacement caused by the propagation of thermoelastic stresses modulates the optical path length or phase of the interferometer sample arm. This path length change can be demodulated by superposing the interferometer probe beam with the reference beam. Let E_1 and E_2 be the electric fields of the interferometer reference and sample beams, respectively, represented by $E_1 = a_1 \exp(i\omega_1 t)$ and $E_2 = a_2 \exp[i(\omega_2 t + (2\pi/\lambda)d)]$. In these expressions, a_1 and a_2 are the electric field amplitudes, ω_1 and ω_2 are the angular frequencies, λ is the wavelength of the source, and d is the change in optical path length of the sample arm. This change in optical path length can be caused, for example, by the surface displacement of the target surface. In this case, the intensity of the interference signal I is [18]:

$$\begin{aligned} I &= (E_1 + E_2)(E_1 + E_2)^* \\ &= a_1^2 + a_2^2 + 2a_1 a_2 \cos\left[(\omega_1 - \omega_2)t - \frac{2\pi}{\lambda}d\right]. \end{aligned} \tag{19.4}$$

The case in which the optical frequency of the reference and measurement arms is identical $(\omega_1 = \omega_2)$ is known as homodyne interferometry. In homodyne interferometry, the interference signal becomes $I = A + B\cos((2\pi/\lambda)d)$, where $A = a_1^2 + a_2^2$ and $B = 2a_1 a_2$. In this case, a minimum of three phase-shifted measurements is required to determine the change in the optical path length d and the unknowns A and B [19]. This phase shifting is usually achieved using a piezoelectric translator to move the reflecting surface in the reference arm of the interferometer by a predefined distance. In Section 19.3, we discuss the use of homodyne interferometry in optoacoustics.

Cases in which $\omega_1 \neq \omega_2$ are known as heterodyne interferometry. This is achieved by modulating the optical frequency of either the reference or sample beam using a frequency-shifting device, such as an acousto-optic modulator (AOM) [20]. The frequency difference $\Delta\omega = |\omega_1 - \omega_2|$ is normally in the radio-frequency range, i.e., on the order of 10–100 MHz. The intensity of the heterodyne interference signal is $I = A + B\cos(\Delta\omega t - (2\pi/\lambda)d)$. This is identical to the homodyne interferometer signal except that the signal is modulated in the time domain with the carrier frequency $\Delta\omega$. Displacement information can be obtained using the so-called superheterodyne technique, by multiplying the interference signal with the reference carrier signal and applying a low-pass frequency filter to the resulting signal [21]. The application of heterodyne interferometry to optoacoustic imaging is detailed in Section 19.4.

The frequency change or Doppler shift in the sample arm of the interferometer produced by the thermoelastic displacement can also be detected using a Fabry–Perot etalon as a spectrum analyzer. The Fabry–Perot interferometer is a multiple-beam interferometer, where a laser beam entering a resonator undergoes multiple reflections within the cavity. Transmission through the resonator depends not only on the cavity properties, but also on the laser frequency. Thus, the signal intensity emerging from the resonator indicates the change in the laser frequency due to the thermoelastic displacement. Confocal Fabry-Perot interferometers use condensing lenses to increase light-gathering capability and can be used with highly scattering surfaces. Application of confocal Fabry-Perot interferometers to optoacoustics is described in Section 19.5.

19.3 OPTOACOUSTICS USING HOMODYNE INTERFEROMETRY

Optical interferometry is classified according to the coherence of the light source, signal modulation and detection (homodyne vs. heterodyne), interference pattern (two-beam, multiple-beam), and geometrical configuration (common-path or two-arm) [22]. The Michelson interferometer, frequently used as an optoacoustic displacement sensor, is a representative two-arm homodyne interferometer, where a monochromatic laser beam is divided and combined by a beam splitter as shown in Figure 19.1a. A disadvantage of this configuration is its low system efficiency, as only half of the light from the laser is reflected towards the detector. This efficiency can be improved by implementing a simple optical isolator consisting of a polarizer and a quarter-wave $(\lambda/4)$ plate. Figure 19.1b displays this modified configuration, where a polarized light source is used and the polarizing beam splitter 1 and two $\lambda/4$ plates are substituted for the simple beam splitter in Figure 19.1a. Light from the laser with 45° polarization state is incident on the polarizing beam splitter 1 and divided into two orthogonal polarization states. The $\lambda/4$ plates in both arms are arranged so that the polarization direction of the returning light is rotated by 90° and directed towards the photo detectors by polarization sensitive beam splitter 1 [23]. Dual detection for noise rejection and signal amplification is usually applied to enhance the signal-to-noise (S/N) ratio. After beam splitter 1, the polarization state of the two beams is orthogonal relative to each other and a half-wave $(\lambda/2)$ plate rotates their polarization axes by 45°. Thus, half of each beam is reflected toward the photo detector 1, while the other half is transmitted through the polarization sensitive beam splitter 2. The $\lambda/2$ plate also retards the reference beam relative to the measurement beam, depending on the polarization axis of beam splitter 2. Thus, the two detected signals are phase-shifted by 180° relative to each other and subtracted for noise stabilization and amplification.

Miniaturization of this arrangement using optical fibers can be achieved by the use of a 2×2 fiber coupler, as shown in Figure 19.2. Such an arrangement has been shown capable of measuring subnanometer surface and bulk displacements associated with optoacoustic pressure waves in methanol and water [24,25]. The output of a laser diode is coupled into a single-mode fiber that is split between the reference and measurement arm at the directional coupler C1. The probe beam reflected from the target interferes with the reference beam that is returned by a fiber loop reflector. Signals from the detector D2 and D3 are opposite in phase and adjusted with gains for dual detection. The amplitude of the difference signal is determined by intentionally changing the reference path length using a piezoelectric phase shifter (PZ) and monitoring the resulting signal. The phase or displacement is obtained in linear relation with the signal on the assumption that the optoacoustic displacement is much less than the wavelength of the laser source. An active phase-control servo system, using the piezoelectric phase shifter, compensates for any low frequency vibration and thermal drift. For excitation of the target, a 1.6-mJ pulse from a Nd:YAG pulse laser, operating at wavelength 1,064 nm with a pulse duration of 180 ns, was focused at one of the foci of a truncated elliptical section, as depicted in Figure 19.3a. A reflective membrane is placed at the second elliptical focus from which the interferometer probe beam is collected. The liquid sample could reside entirely below the membrane for the detection of the surface displacement. Alternatively, the membrane could be placed within a liquid sample to measure the displacement within the bulk of the liquid target. Also shown in Figure 19.3 is a comparison between the surface (b) and bulk (c) displacements associated with the thermoelastic response of the water target. The surface displacement is $2\times$ larger than the bulk displacements, as the thermoelastic pressure drops to zero at the liquid-air interface [26].

Homodyne interferometry is also utilized using fiber optic sensors to measure the average pressure over the fiber face. However, these systems must be calibrated in order to obtain quantitative information [27]. The quantitative measurement of pressure waves using intrinsic fiber sensors is difficult, because the actual amplitude of the detected signal

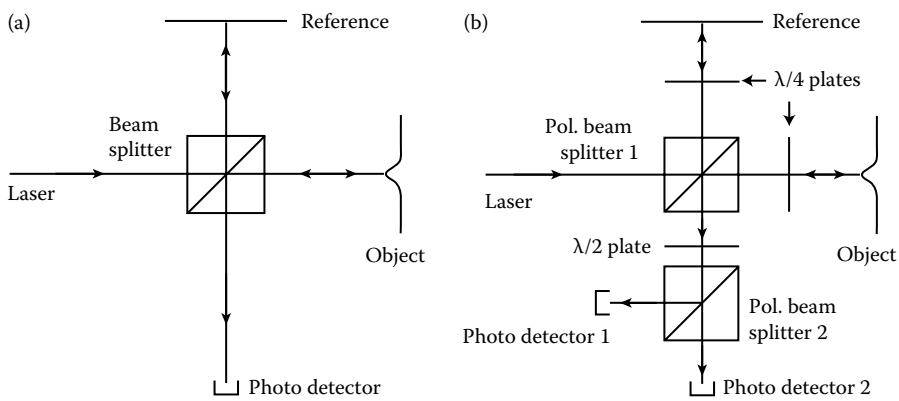

FIGURE 19.1 (a) Schematic of a Michelson interferometer for measuring optoacoustic displacement. (b) Michelson interferometer employing optical isolation and dual detection for increased signal efficiency.

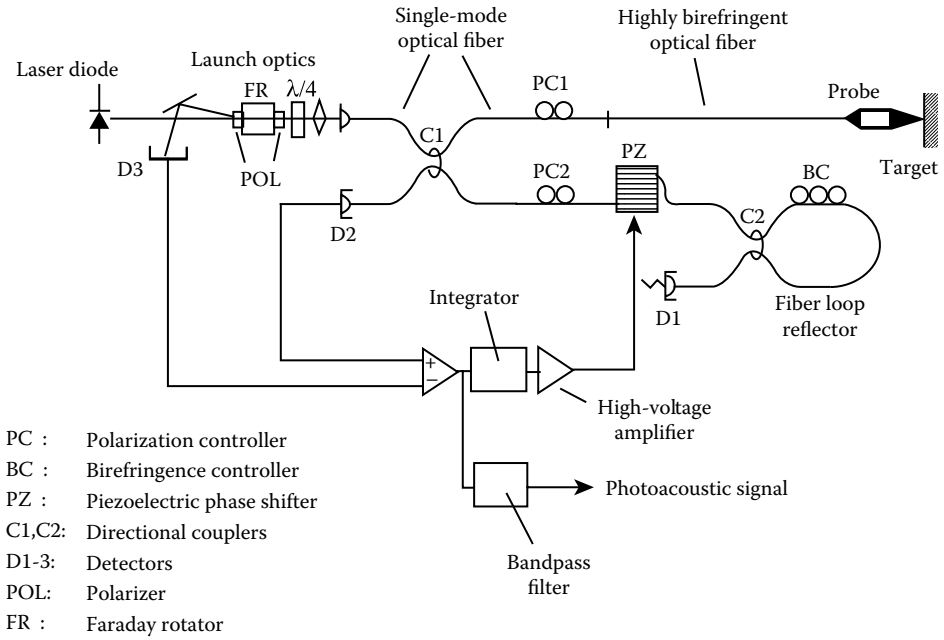

FIGURE 19.2 Schematic of the optical-fiber interferometer for optoacoustic displacement measurement. (Reproduced from Hand, D.P., S. Freeborn, P. Hodgson, T.A. Carolan, K.M. Quan, H.A. Mackenzie, and J.D.C. Jones, *Opt. Lett.* 20(2):213–15, 1995. With permission.)

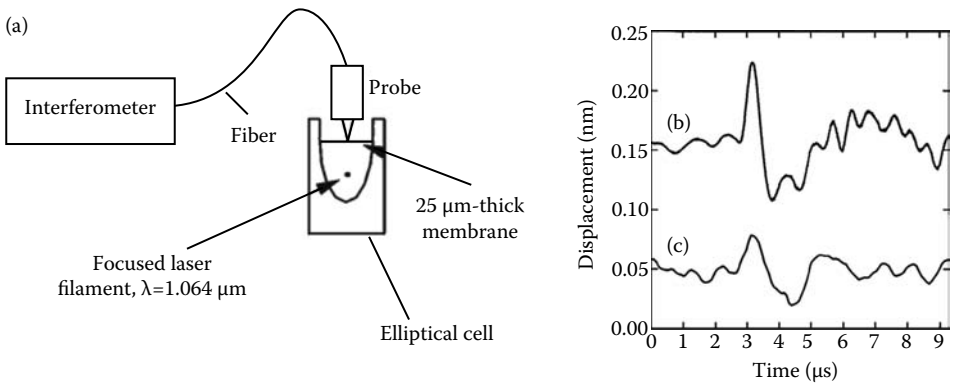

FIGURE 19.3 (a) Experimental arrangement for liquid optoacoustic displacement. (b) Surface and (c) bulk displacements produced by an optoacoustic wave in water. (Reproduced from Hand, D.P. S., Freeborn, P. Hodgson, T.A. Carolan, K.M. Quan, H.A. Mackenzie, and J.D.C. Jones, *Opt. Lett.* 20(2):213–15, 1995. With permission.)

depends on many factors, including the acoustic frequency, the length of sensing fiber, and angle of incidence of the pressure wave on the fiber face. Calibration is usually performed by modulating the path length of the reference arm and monitoring the interferometer signal [28]. On the other hand, intrinsic fiber interferometers can be assembled easily to provide multichannel optoacoustic probes for catheter applications [29]. A metal-coated single-mode fiber sensor, based on a Michelson interferometer, has also been applied for measuring shock waves with a high damage threshold level and is not feasible generally with conventional hydrophones [30]. Low coherence sources, such as femtosecond lasers, have also been used for homodyne interferometry in depth-resolved optoacoustic detection through turbid media [31–34].

19.4 OPTOACOUSTIC TOMOGRAPHY USING HETERODYNE INTERFEROMETRY

Optoacoustic displacement sensors utilizing homodyne interferometry have a flat frequency response and are thus susceptible to low-frequency noise. In practical applications, interferometers measuring the surface velocity instead of displacement demonstrate a low sensitivity to ambient noise, as the sensitivity of these systems is proportional to the frequency of the acoustic pressure wave [35]. Phase modulation of the reference arm in the interferometer through the translation of the reference-reflecting surface at constant velocity is a simple frequency-shifting technique. This allows for the determination of both the direction and amplitude of the thermoelastic displacement [13,36]. Several papers have examined the use

of heterodyne Michelson interferometry and compared displacement measurements with theoretical predictions obtained by solving the thermoelastic wave equation to determine the physical properties of hydrated tissues [13,17,36,37].

AOM can also be used for optical frequency shifting and have the advantage of frequency tunability and better stability without moving parts [38]. Yablon and coworkers [20] developed a heterodyne Mach-Zehnder interferometer using an AOM for beam splitting and 110 MHz-frequency shifting. This technique was applied for the examination of the time-resolved surface displacement produced by pulsed ArF excimer laser irradiation of corneal tissue to determine its optical absorption coefficient. This system was also used by Payne and coworkers for the precise determination of optical attenuation depths of both diffusively and specularly reflecting turbid targets [39]. Optoacoustic tomography of heterogeneous targets is possible by measuring transient displacements at multiple locations and processing the data with appropriate image reconstruction algorithms. The remainder of this section is devoted to the results of our group in using this heterodyne Mach-Zehnder interferometer for optoacoustic tomography [5,40,41].

19.4.1 Experimental Setup

Figure 19.4 provides the schematic of an optoacoustic imaging system using a heterodyne Mach-Zehnder interferometer [42], where a Q-switched Nd:YAG laser delivers 5-ns pulses at wavelength 1,064 or 532 nm to the sample, and the interferometer measures the resulting thermoelastic surface displacement. The interferometer uses a linearly polarized He-Ne laser ($\lambda = 632.8$ nm), whose output is split by an AOM driven at 110 MHz. A portion of the He-Ne laser beam travels undisturbed through the AOM and is delivered to the target surface, while the remaining portion of the beam is deflected into several frequency-shifted beams. One of the first-order frequency-shifted beams ($\Delta f = f_{AOM} = 110$ MHz) is picked off by a mirror and becomes the reference beam of the interferometer. The unshifted measurement beam passes through a $\lambda/4$ plate to rotate its polarization direction by a total of 90° after its roundtrip travel to the sample, and is then reflected by the polarization sensitive beam splitter. The interference signal is formed at the 50/50 beam splitter and divided into two paths for balanced dual detection using Si PIN photodiodes. The combined photodiode signal is amplified using a broadband low-noise amplifier and recorded by a digital oscilloscope. For automated operation, the personal computer controls the pump laser and the two translation stages are used to position the sample. The time-resolved surface displacement $u(t)$ is directly proportional to the time-resolved phase difference between the interferometer signal $\Phi_{INT}(t)$ and the AOM driving signal $\Phi_{AOM}(t)$:

$$u(t) = \frac{\lambda[\Phi_{INT}(t) - \Phi_{AOM}(t)]}{4\pi}, \tag{19.5}$$

where λ is the wavelength of the interferometer beam and

$$\Phi_{AOM,INT}(t) = \arctan\left\{\frac{H\left[I_{AOM,INT}(t)\right]}{I_{AOM,INT}(t)}\right\}, \tag{19.6}$$

where H denotes the Hilbert transform and $I_{AOM,INT}(t)$ denotes the raw digitized voltages of the AOM driving signal and the interferometer signal, respectively. A fiber-optic implementation of this system for the direct measurement of shock waves has also been accomplished, as shown in Figure 19.5 [43].

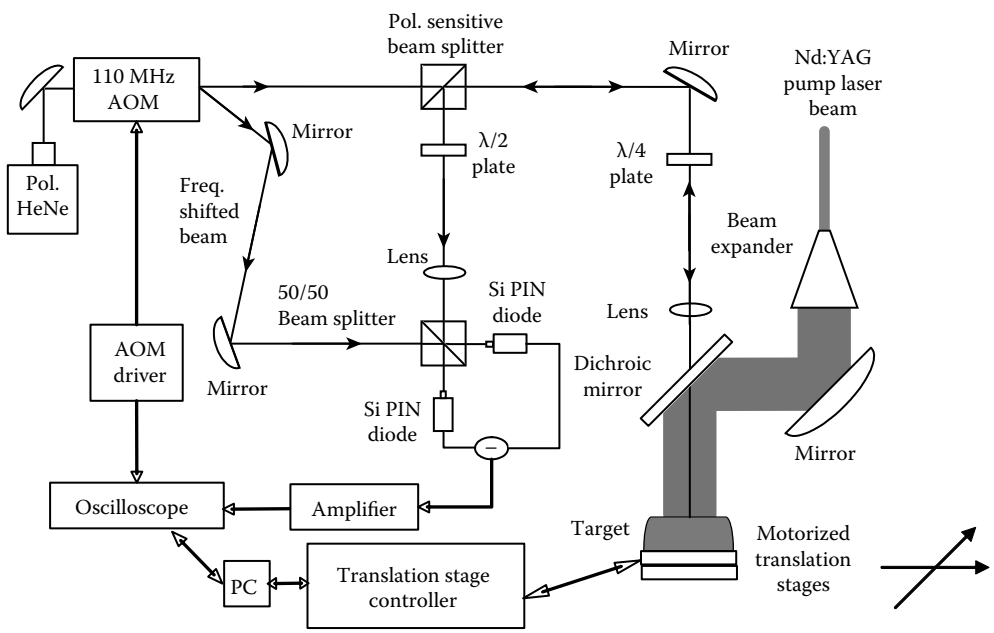

FIGURE 19.4 Schematic of the heterodyne Mach-Zehnder interferometer system for optoacoustic tomography.

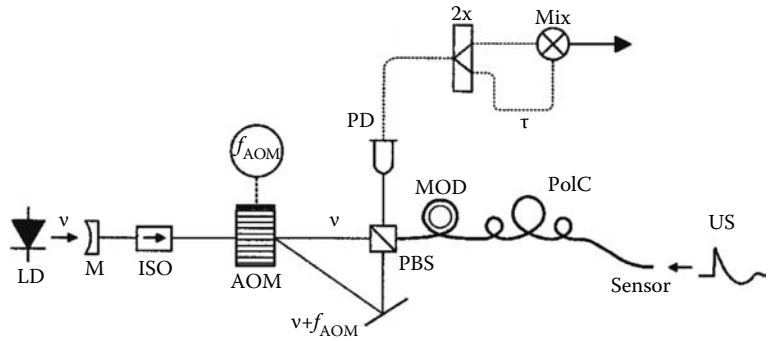

FIGURE 19.5 Heterodyne fiber-tip sensor system: LD, laser diode with frequency v; M, partly reflecting mirror; ISO, optical isolator; AOM, acousto-optic modulator with driving frequency f_{AOM}; PBS, polarization beam splitter; MOD, piezoelectric transducer ring phase modulator; PolC, polarization controller; US, ultrasound signal; PD, photodiode; 2×, in-phase 1:1 power divider; Mix, double-balanced mixer; τ , delay line. (Reproduced from Bruinsma, A.J.A., and J.A. Vogel, *Appl. Opt.* 27(22), 4690–95, 1988. With permission.)

19.4.2 Image Reconstruction Algorithm

A simple delay and sum beam-forming algorithm can be applied for reconstructing subsurface optical heterogeneities from thermoelastic surface displacement profiles measured at multiple locations [12,44]. The target volume is divided into small volume elements (voxels), each of which is evaluated as a potential source of the measured thermoelastic disturbance. The delay and sum method determines the acoustic source intensity at each voxel by finding the time window of every trace corresponding to the distance between the voxel and the detection point, and performing a weighted summation over all displacement signals. This is given by the expression [45]:

$$I(\mathbf{r}) = \frac{\sum_i w_i^d \left\langle S_i \left[\frac{(\mathbf{r}_i^d - \mathbf{r}) - l/2}{v_s} : \frac{(\mathbf{r}_i^d - \mathbf{r}) + l/2}{v_s} \right] \right\rangle}{\sum_i w_i^d}, \quad (14.7)$$

where $\mathbf{r}$ is the location in the imaged volume, $I(\mathbf{r})$ is the acoustic source intensity corresponding to location $\mathbf{r}$, $\sum_i$ denotes a sum over all the detection points, w_i^d is a detector specific weighting factor, $S_i(t)$ is the time-resolved surface displacement signal from the ith measurement location, $\mathbf{r}_i^d$ is the location of the ith detector, v_s is the speed of sound, and l is the voxel size. The operator ":" denotes the set of discrete displacements acquired within the time window of interest, and "< >" denotes averaging the signal over the specified time interval that, in this case, corresponds to the transit time across the voxel in question. This method assigns a high-source strength to a voxel if prominent displacement features are present within the corresponding time windows of all traces. However, even voxels without an acoustic source may be assigned a finite acoustic source intensity due to the presence of "ghost" acoustic sources, i.e., an acoustic source present elsewhere within the system that is nonetheless equidistant from the detector location. Such "ghost" acoustic sources are the origin of "arcing" artifacts seen in images that are reconstructed using simple backprojection algorithms.

To improve the reconstructed image quality, a set of weights w_i^d can be applied to the measured signal to compensate for various aspects of the thermoelastic stress wave propagation. For example, weights can be applied to compensate for directional variations of the detector sensitivity [12]:

$$w_i = 1/\cos(\alpha_i), \quad (19.8)$$

where α is the angle between the line connecting the measurement location $\mathbf{r}_i^d$ with the current voxel location $\mathbf{r}$ and the inward pointing normal passing through the measurement location $\mathbf{r}_i$. Weighting can also be used to compensate for geometrical attenuation of the acoustic wave as it travels from the acoustic source to the detector:

$$w_i = \| \mathbf{r}_i^d - \mathbf{r} \|^n, \quad (19.9)$$

where $n = 1$–2. The coherence weighting approach introduced by Liao and coworkers [46] can reduce arcing artifacts and improve the S/N ratio of the reconstructed image. The coherence-weighted acoustic source intensity I_{CF} corresponding to location $\mathbf{r}$ is given by:

$$I_{CF}(\mathbf{r}) = \mathrm{CF}(\mathbf{r}) \cdot I(\mathbf{r}), \quad (19.10)$$

with

$$\mathrm{CF}(\mathbf{r}) = \frac{\left| \sum_{i=1}^{N} \langle S_i(\mathbf{r}) \rangle \right|^2}{N \sum_{i=1}^{N} \left| \langle S_i(\mathbf{r}) \rangle \right|^2}, \quad (19.11)$$

where N is the number of measurement locations, CF is the coherence factor for the same location, and $\langle S_i(\mathbf{r}) \rangle$ is the time-averaged displacement signal corresponding to the voxel centered at $\mathbf{r}$. The coherence factor is maximized only when *all* the detectors register a strong signal in the time window under examination. However, a large variation in the measured signal across detectors, which occurs when a ghost acoustic source is present, results in a large standard deviation and reduces the coherence factor [46].

Consequently, multiplication by CF(**r**) reduces the acoustic source intensity $I(\mathbf{r})$ if the location **r** does not contain a real acoustic source, because only a subset of detectors will register a displacement signal within the time windows under examination.

19.4.3 Tissue Phantom Results

Tissue phantoms were fabricated using a 2% Intralipid solution ($\mu_s' = 1\ \text{mm}^{-1}$ and $\mu_a = 0.012\ \text{mm}^{-1}$ at wavelength 1,064 nm) with simulated vessels composed of polyimide tubes with a 160 μm outer diameter and 20 μm wall thickness submerged at a depth of 4–8 mm. A solution of India ink with $\mu_a = 0.5\ \text{mm}^{-1}$ was circulated through the tubes using a syringe pump to simulate the absorption of whole blood at the 1,064-nm wavelength. A pulsed laser with 22.5-mm beam diameter, 5-ns pulse duration at 1,064 nm, provided an incident radiant exposure of $\leq 120\ \text{mJ/cm}^2$. At this wavelength, the polyimide tubes are essentially transparent, and their contribution to the displacement signal is negligible.

Figure 19.6 shows a set of time-resolved surface displacement traces collected at several locations on the surface of a phantom containing two tubes spaced 250 μm apart and placed at a depth of 8.1 mm. The gradual expansion of the sample over the microsecond time scale is due to background optical absorption of the Intralipid solution. The polyimide tubes generate displacement features at times corresponding to the acoustic transit between each tube and the position of the interferometer beam. When $r = 0$, there is only a small difference in the transit times from each tube to the detector location, and this results in a single broadened displacement peak. As the measurement position moves laterally, the difference in the transit time between each of the tubes and the detector location increases. Thus, the displacements produced by the individual tubes begin to separate in time, and is most notable at $r = 12$ mm.

To form a 2-D image of such phantoms, measurements were taken at 65 locations spanning the interval $r \in [-16,16]$ mm at 0.5-mm increments along a line-segment perpendicular to the tube axes. Reconstructed images from two tissue phantoms containing two parallel polyimide tubes spaced 200 μm apart and placed at depths of 4 and 7.75 mm are shown in Figure 19.7, along with line-scans through the perceived centers of the tubes. The line-scans show clearly that these tubes are resolved at depths approaching 8 mm in highly turbid media. The arcing artifact presented in these images is intrinsic to the reconstruction algorithm, especially when displacement measurement can only be taken in a "backscattering" geometry. However, the artifact can be reduced by increasing the number and spatial density of the measurement positions.

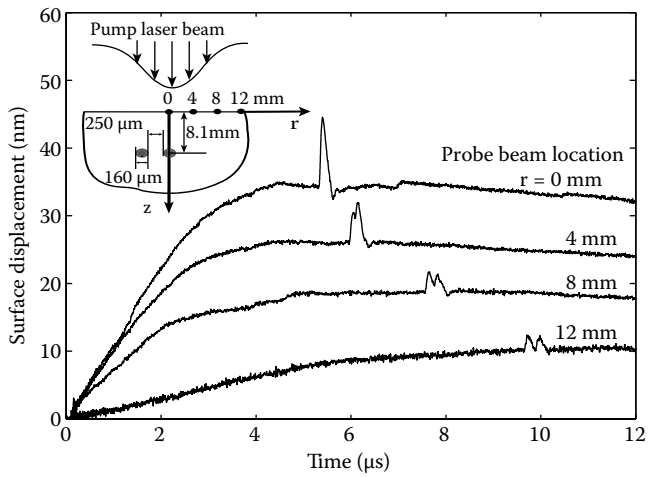

FIGURE 19.6 Displacement traces recorded at several positions on the surface of a phantom containing two 160 μm diameter polyimide tubes spaced at a wall-to-wall distance of 250 μm and located at a depth of 8.1 mm. Probe beam locations are given by the filled circles shown on the phantom surface.

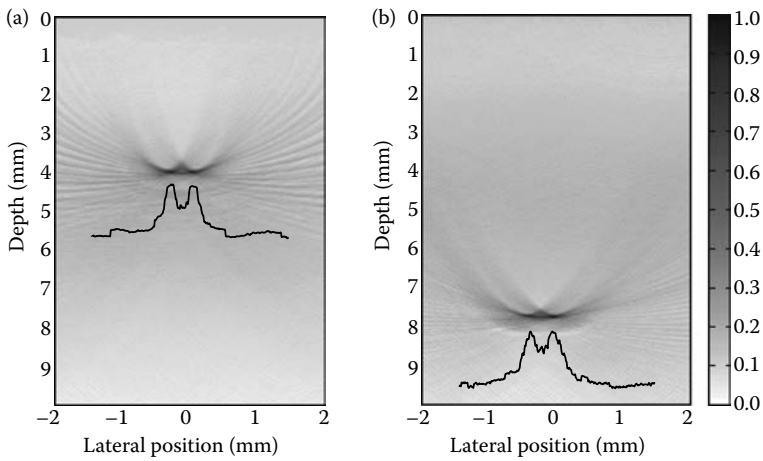

FIGURE 19.7 Image reconstructions of phantoms containing two 160-μm diameter polyimide tubes spaced at a wall-to-wall distance of 200 μm and located at depths of (a) 4 and (b) 7.75 mm. Line scans shown are taken through the perceived centers of the tubes.

19.4.4 Animal Model Results

Experiments were performed using the same system to image the vascular network of a rat brain [45]. To mimic the optical scattering produced by the rat skull and scalp, the brain was immersed in a dilute (0.2%) Intralipid solution in a container with the brain 2 mm below the Intralipid surface. A Q-switched Nd:YAG laser, operating at 532 nm with a 5-ns pulse duration and 18 mm beam diameter (after expansion), was used to irradiate the sample with radiant exposure of 80 mJ/cm^2. The displacement signals were high-pass filtered to enhance the prominence of high-frequency displacement features that are produced by the small vessels. Figure 19.8 shows a comparison between a photograph of the upper surface of the brain prior to immersion in the Intralipid and a reconstructed image using the pulsed optoacoustic interferometric spectroscopy and imaging (POISe) system. The measurement array spanned a 20×20-mm area, with measurements taken at locations spaced 0.5 mm apart, resulting in 1,681 distinct measurement locations. Four displacement traces were acquired at each location, requiring roughly 25 min for the entire data acquisition process. The reconstructed volume measures 15×15×10 mm and consists of 50×50×50 μm volume elements for a total 300×300×200 voxels. Blood vessels as small as 50 μm in diameter, shown in Figure 19.8a, are clearly visible in the reconstructed images albeit with a larger size of ~100 μm.

An important issue is the interrelationship between the reconstructed image quality and field-of-view with respect to the span of the measurement. Figure 19.9 presents the impact of different variations in the measurement area and density on the image reconstruction shown in Figure 19.8. In all the images shown, the reconstructed volume measures 15×15×10 mm and contains 300×300×200 voxels, each 50×50×50 μm in size. The images were reconstructed with high-pass filtering and the delay and sum beam-forming algorithm to which the distance and directivity corrections were applied.

Figure 19.9a is identical to Figure 19.8b and is reconstructed from a measurement array 20×20-mm in area, with measurements taken at 0.5-mm intervals. Figure 19.9b

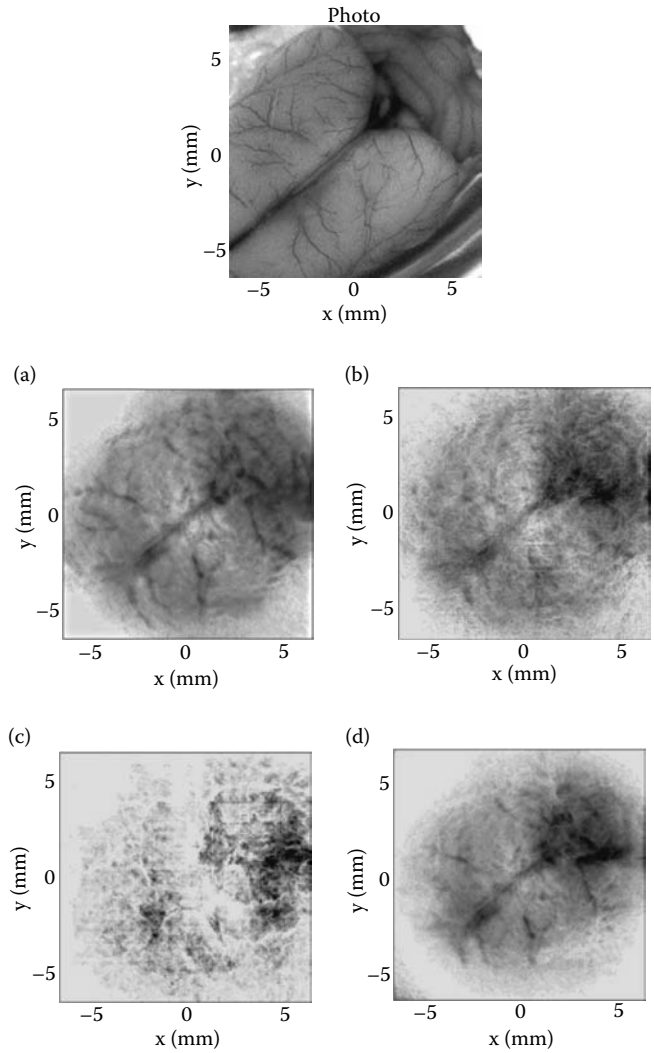

FIGURE 19.9 Influence of variations in the size of the scanning area and measurement density on the image reconstruction quality. (a) Reconstructed image of the rat brain when measurements were taken over 20×20 mm at 0.5-mm intervals. (b) Image with measurements taken over 20×20 mm at 1-mm intervals. (c) Image with measurements taken over 20×20 mm at 2-mm intervals. (d) Image with measurements taken over 13×13 mm at 0.5-mm intervals.

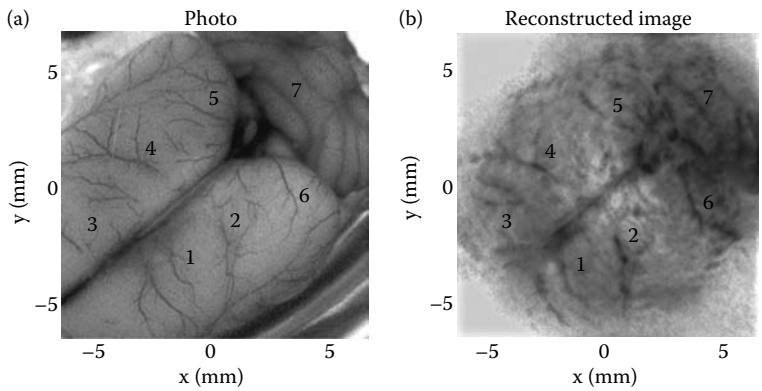

FIGURE 19.8 (a) A photograph of the upper surface of the brain prior to Intralipid immersion, (b) a reconstructed optoacoustic image of the rat brain under a 2-mm layer of 0.2% Intralipid.

and c show the image reconstruction using measurement data acquired over the same 20×20-mm area, but with measurements taken at 1- and 2-mm intervals, respectively. The image reconstruction shown in Figure 19.9b shows that a reduction in measurement density, accomplished by expanding the distance between the measurement locations to 1 mm, results in a loss of the small ($\lesssim$100 μm) features. Figure 19.9c, in which the measurement spacing was expanded to 2 mm, exhibits a marked loss in detail to the point that none of the main features visible in the photograph can be identified in the POISe image reconstruction. Figure 19.9d, in which the measurement density was retained at 0.5-mm spacing but the measurement area was reduced from 20×20 mm to 13×13 mm, results in a proportional reduction in the field-of-view. The small blood vessels are still visible near the center of the image, but are missing towards the edges of the reconstructed area. This result indicates that the spatial array of displacement measurements must extend at least 30% beyond the area to be reconstructed.

19.5 OPTOACOUSTICS USING CONFOCAL FABRY-PEROT INTERFEROMETRY

The ability of interferometers to measure optoacoustic displacements degrades with increasing roughness of the object surface, as surface roughness disturbs the reflected wavefront resulting in a speckle pattern. While the contribution of the volume scattering is negligible when using a confocal imaging scheme and effectively rejected in heterodyne interferometers, the speckles emanating from the rough surface combine incoherently at the detector and thus degrade the S/N ratio of the detected signal [47]. Nevertheless, the two-beam interferometers described in Sections 19.3 and 19.4 are still capable of detecting optoacoustic displacements at rough surfaces by receiving back-scattered light corresponding to one of the brightest speckle points. In scanning applications, however, the traversal of the laser beam over the sample surface can lead to changes in the spatial distribution of the speckle pattern and result in poor detection sensitivity unless optical realignment of the interferometer is accomplished dynamically [48]. Multiple-beam interferometers, such as the confocal Fabry-Perot interferometer (CFPI), can analyze many speckles simultaneously and are much less sensitive to surface roughness. The CFPI is a velocity measurement interferometer, which makes it insensitive to low-frequency noise. The low optical efficiency of the CFPI, due to the highly reflecting cavity surface, can be overcome by using higher incident laser powers.

A fiber optic implementation of a CFPI is shown in Figure 19.10, where controlled generation of pressure waves by a piezoelectric transducer was measured to assess system performance [35]. The optical signal reflected from the target surface is received through a multimode fiber and delivered to a CFPI cavity whose center is conjugate with the laser spot on the object surface. The thermoelastic displacement modulates the optical frequency via the Doppler effect, and the CFPI demodulates the variation to provide an intensity-modulated signal. For best sensitivity, the laser frequency is set at the half maximum point of the response curve that is achieved by controlling the thickness of the cavity with a PZT pusher and the detector D_1. The size of a circular fringe at the detector D_2 is determined by the third-order spherical aberration of the system. The fringe intensity depends on the cavity parameters [4]. Two identical spherical mirrors, which form the resonator of the CFPI, are aligned such that incident optical ray is collinear with the axis of the device and traverses the cavity four times before interfering with itself. The length of the cavity and the reflectivity of the cavity mirrors determine the efficiency and bandwidth of the pressure wave detection. Hamilton and coworkers used a CFPI with a scanning system to image tissue phantoms modulated with ultrasonic transducer [49]. Sakadžić and coworkers have used a CFPI for ultrasound-modulated optical tomography [50]. Hoyes and coworkers reported the use of a CFPI to image material defects by detecting the irradiant thermoelastic generation of stress waves initiated by Q-switched Nd:YAG laser [47]. This scheme can also be applied to targets of biomedical interest.

19.6 CONCLUSIONS AND FUTURE DIRECTIONS

Optoacoustic image reconstruction based on the time-resolved measurement of surface displacement has employed interferometric approaches well known in the optical metrology community. In general, these approaches do not require acoustic coupling between the target surface and the detector and they are all point displacement sensors. High bandwidth photo detectors convey time-rich interferometric signals, and scanning mechanisms such as translation stages or galvanomirrors enable the acquisition of measurements at multiple locations. An array of time-resolved displacement measurements acquired at multiple spatial locations on the target surface can be used to determine the thermophysical and optical properties of the sample and to form high-resolution images.

Current interferometric systems require image acquisition times on the order of tens of minutes to scan the surface of the target, and are not yet adequate to monitor rapid physiological changes. The reduction of image acquisition time is thus an important hurdle that the optoacoustic-imaging community faces. A reduction of image acquisition time may be obtained by using multibeam interferometry combined with parallel optical detection. Unlike piezoelectric transducers in which array detection has long been utilized for fast and high-resolution imaging, parallel signal acquisition and processing using optical interferometry is still under development. Two-dimensional photo detector arrays can be used to capture interference signals at multiple locations. However, the number of sensors is limited to a few hundred and the associated electronics are costly [51,52]. The use of a line CCD camera synchronized with a sinusoidally modulated pump laser can detect optoacoustic displacement effectively, but may not be appropriate for pulsed optoacoustics in biomedical applications [53–55]. Visualization of the spatially resolved response Fabry-Perot polymer sensor using a standard CCD camera

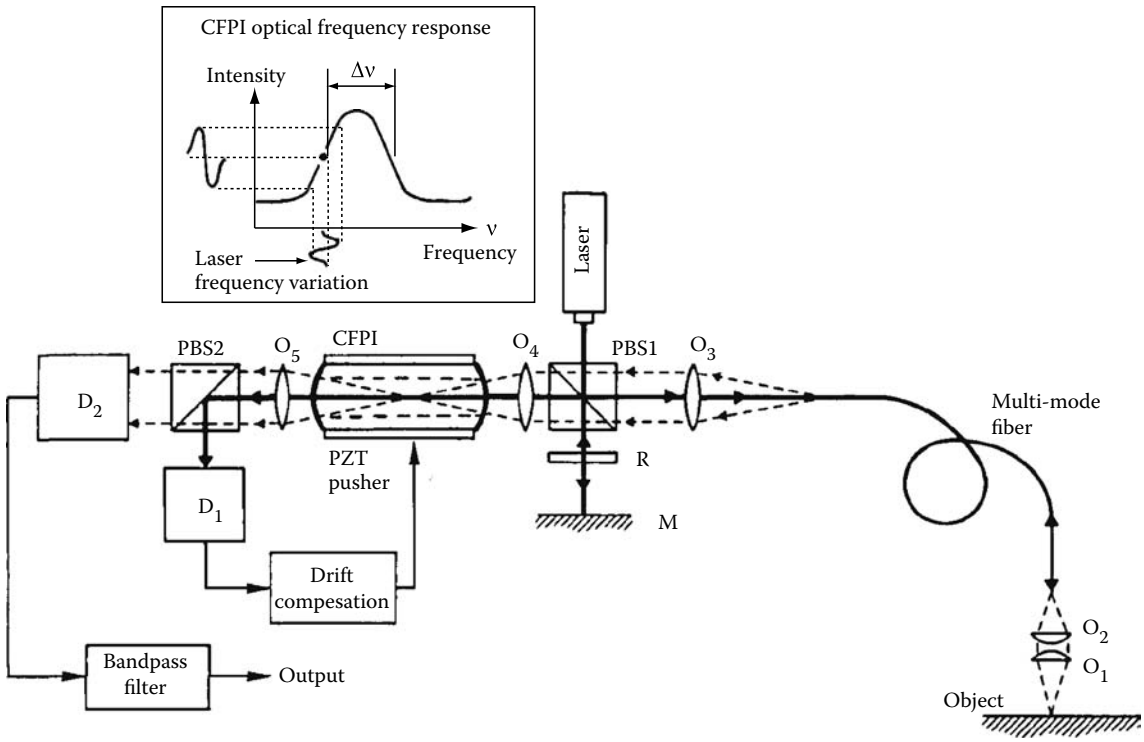

FIGURE 19.10 Schematic diagram of a fiber confocal Fabry-Perot interferometer system: PBS1 and PBS2, polarizing beam splitter; R, λ/4 retarder; M, mirror; O_{1-5}, collimating lenses; D_1 and D_2, photodiodes. (Reproduced from Bruinsma, A.J.A., and J.A. Vogel, *Appl. Opt.* 27(22):4690–695, 1988. With permission.)

is an affordable method to increase the measurement speed [56]. A time-gated CCD camera may be used, taking advantage of its fast shuttering capability and the high resolution of a standard CCD camera. Paltauf and coworkers demonstrated the use of a gated CCD camera, where variations of optical reflectance due to optoacoustic pressure were measured using the Fresnel formula [8,57,58]. However, this system suffers from low sensitivity. Improvements in the speed, sensitivity, and stability of optical interferometers while exploiting its ability for precise, noncontact detection, will be the key to enable the translation of optoacoustic imaging via optical interferometry to clinical application.

REFERENCES

1. Korpel, A., L.J. Laub, and H.C. Sievering. 1967. Measurement of acoustic surface wave propagation characteristics by reflected light. *Appl. Phys. Lett*. 10(10):295–97.
2. Whitman, R.L., and A. Korpel. 1969. Probing of acoustic surface perturbations by coherent light. *Appl. Opt.* 8(8):1567–76.
3. Kline, R.A., R.E. Green, and C.H. Palmer. 1978. Comparison of optically and piezoelectrically sensed acoustic-emission signals. *J. Acoust. Soc. Am.* 64(6):1633–39.
4. Monchalin, J.P. 1986. Optical-detection of ultrasound. *IEEE Trans. Ultrason. Ferroelectr. Freq. Control* 33(5):485–99.
5. Carp, S.A., A. Guerra, S.Q. Duque, and V. Venugopalan. 2004. Optoacoustic imaging using interferometric measurement of surface displacement. *Appl. Phys. Lett*. 85(23):5772–74.
6. Beard, P.C., and T.N. Mills. 1996. Extrinsic optical-fiber ultrasound sensor using a thin polymer film as a low-finesse Fabry-Perot interferometer. *Appl. Opt.* 35(4):663–75.
7. Harris, G.R. 2005. Progress in medical ultrasound exposimetry. *IEEE Trans. Ultrason. Ferroelectr. Freq. Control* 52(5):717–36.
8. Paltauf, G., H. Schmidt-Kloiber, K.P. Köstli, and M. Frenz. 1999. Optical method for two-dimensional ultrasonic detection. *Appl. Phys. Lett*. 75(8):1048–50.
9. Niederhauser, J.J., D. Frauchiger, H.P. Weber, and M. Frenz. 2001. Real-time optoacoustic imaging using a Schlieren transducer. *Appl. Phys. Lett*. 81(4):571–73.
10. Xu, M.H., and L.H.V. Wang. 2006. Photoacoustic imaging in biomedicine. *Rev. Sci. Instrum.* 77(4):041101.
11. Sigrist, M.W., and F.K. Kneubuhl. 1978. Laser-generated stress waves in liquids. *J. Acoust. Soc. Am*. 64(6):1652–63.
12. Hoelen, C.G.A., and F. F.M. de Mul. 2000. Image reconstruction for photoacoustic scanning of tissue structures. *Appl. Opt.* 39(31):5872–83.
13. Itzkan, I., D. Albagli, M.L. Dark, L.T. Perelman, C. von Rosenberg, and M. S. Feld. 1995. The thermoelastic basis of short pulsed-laser ablation of biological tissue. *Proc. Nat. Acad. Sci. USA* 92(6):1960–64.
14. Boley, B.A., and J.H. Weiner. 1960. *Theory of thermal stresses*. New York: John Wiley.
15. Nowacki, W. 1986. *Thermoelasticity*, 2nd edn. Oxford: Pergamon.
16. Dubois, M., F. Enguehard, L. Bertrand, M. Choquet, and J.P. Monchalin. 1994. Modeling of laser thermoelastic generation of ultrasound in an orthotropic medium. *Appl. Phys. Lett*. 64(5):554–556.
17. Dark, M.L., L. T. Perelman, I. Itzkan, J.L. Schaffer, and M.S. Feld. 2000. Physical properties of hydrated tissue determined by surface interferometry of laser-induced thermoelastic deformation. *Phys. Med. Biol*. 45(2):529–539.

18. Hecht, E. 1998. Interference. In *Optics*, 3rd edn., Chapter 9, 378–81. Reading, MA: Addison Wesley.
19. Schreiber. H., and John H. Bruning 1992. Phase shifting Interferometry. In *Optical shop testing*, 2nd edn., ed. Daniel Malacara, Chapter 14, 518–32. New York: Wiley-Interscience.
20. Yablon, A.D., N.S. Nishioka, B.B. Mikić, and V. Venugopalan. 1999. Measurement of tissue absorption coefficients by use of interferometric photothermal spectroscopy. *Appl. Opt.* 38(7):1259–72.
21. Gåsvik, K.J. 1995. Interference. In *Optical metrology*, 2nd edn., Chapter 3, 44–45. Chichester, UK: Wiley.
22. Hariharan, P. 2003. *Optical interferometry*, 2nd end. San Diego, CA: Academic Press.
23. Mezrich, R., D. Vilkomerson, and K. Etzold. 1976. Ultrasonic-waves – their interferometric measurement and display. *Appl. Opt.* 15(6):1499–505.
24. Hand, D.P., P. Hodgson, T.A. Carolan, K.M. Quan, H.A. Mackenzie, and J.D.C. Jones. 1993. Detection of photoacoustic waves in liquids by fiber optic interferometry. *Opt. Commun.* 104(1–3):1–6.
25. Hand, D.P., S. Freeborn, P. Hodgson, T.A. Carolan, K.M. Quan, H.A. Mackenzie, and J.D.C. Jones. 1995. Optical-fiber interferometry for photoacoustic-spectroscopy in liquids. *Opt. Lett.* 20(2):213–15.
26. Paltauf, G., and P.E. Dyer. 2003. Photomechanical processes and effects in ablation. *Chem. Rev*. 103(2):487–518.
27. Lamela, H., V. Cunningham, C. Macia-Sanahuja, J.A. Garcia Souto, and P. Acedo. 2006. Analysis of photoacoustic signal frequencies in deep tissue phantoms using high-sensitive interferometric optical sensors. In *Proceedings of SPIE*, Vol. 6086, eds. A.A. Oraevsky and L.V. Wang, 608610. Bellingham, WA: SPIE.
28. Fomitchov, P., T.W. Murray, and S. Krishnaswamy. 2002. Intrinsic fiber-optic ultrasonic sensor array using multiplexed two-wave mixing interferometry. *Appl. Opt.* 41(7):1262–66.
29. Fomitchov, P.A., A.K.Kromine, and S. Krishnaswamy. 2002. Photoacoustic probes for nondestructive testing and biomedical applications. *Appl. Opt.* 41(22):4451–59.
30. Koch, C., W. Molkenstruck, and R. Reibold. 1997. Shock-wave measurement using a calibrated interferometric fiber-tip sensor. *Ultrasound Med. Biol*. 23(8):1259–66.
31. Yu, P., D.D. Nolte, and M.R. Melloch. 2002. Laser-based ultrasound detection through turbid media. In *Proceedings of SPIE*, Vol. 4618, ed. A.A. Oraevsky, 128–36. Bellingham, WA: SPIE.
32. Yu, P., L. Peng, D.D. Nolte, and M. R. Melloch. 2003. Ultrasound detection through turbid media. *Opt. Lett.* 28(10):819–21.
33. Telenkov, S.A., D.P. Dave, and T.E. Milner. 2003. Low-coherence interferometric detection of photo-thermal and photo-acoustic effects in tissue. In *Proceedings of SPIE*, Vol. 4960, ed. A. A. Oraevsky, 142–46. Bellingham, WA: SPIE.
34. Telenkov, S.A., D.P. Dave, S. Sethuraman, T. Akkin, and T.E. Milner. 2004. Differential phase optical coherence probe for depth-resolved detection of photothermal response in tissue. *Phys. Med. Biol*. 49(1):111–19.
35. Bruinsma, A.J.A., and J.A. Vogel. 1988. Ultrasonic noncontact inspection system with optical fiber methods. *Appl. Opt.* 27(22):4690–95.
36. Albagli, D., M. Dark, L.T. Perelman, C. von Rosenberg, I. Itzkan, and M. S. Feld. 1994. Photomechanical basis of laser-ablation of biological tissue. *Opt. Lett.* 19(21):1684–86.
37. Albagli, D., M. Dark, L. Perelman, C. von Rosenberg, I. Itzkan, and M.S. Feld. 1994. Laser-induced thermoelastic deformation: A three-dimensional solution and its application to the ablation of biological tissue. *Med. Phys*. 21(8):1323–31.
38. Saleh, B.E.A., and M.C. Teich. 1991. Acousto-optics. *Fundamentals of photonics*, 799–831. Wiley Series in Pure and Applied Optics. New York: Wiley-Interscience. Acousto-Optics
39. Payne, B.P., V. Venugopalan, B.B. Mikić, and N.S. Nishioka. 2003. Optoacoustic determination of optical attenuation depth using interferometric detection. *J. Biomed. Opt*. 8(2):264–72.
40. Carp, S.A., and V. Venugopalan. 2005. 3D interferometric optoacoustic imaging. In *Proceedings of SPIE*, Vol. 5697, eds. A.A. Oraevsky and L.V. Wang, 307–12. Bellingham, WA: SPIE.
41. Carp, S.A., and V. Venugopalan. 2007. Optoacoustic imaging based on the interferometric measurement of surface displacement. *J. Biomed. Opt*. 12(6):064001.
42. Carp, S.A., A. Guerra III, S.Q. Duque Jr., and V. Venugopalan. 2004. POISe: Pulsed optoacoustic interferometric spectroscopy and imaging. In *Proceedings of SPIE*, Vol. 5320, eds. A. A. Oraevsky and L. V. Wang, 214–21. Bellingham, WA: SPIE.
43. Koch, C. 1999. Measurement of ultrasonic pressure by heterodyne interferometry with a fiber-tip sensor. *Appl. Opt.* 38(13):2812–19.
44. Johnson, D.H., and D.E. Dudgeon. 1993. *Array signal processing: Concepts and techniques*, 1st edn. Englewood Cliffs, NJ: Prentice Hall PTR.
45. Carp. S.A. 2005. Pulsed optoelastic interferometric spectroscopy and imaging. PhD thesis, University of California.
46. Liao, C.K., M.L.Li, and P.C.Li. 2004. Optoacoustic imaging with synthetic aperture focusing and coherence weighting. *Opt. Lett.* 29(21):2506–508.
47. Hoyes, J.B., Q. Shan, and R.J. Dewhurst. 1991. A noncontact scanning system for laser ultrasonic defect imaging. *Measure. Sci. Technol*. 2(7):628–34.
48. Monchalin, J.P. 1985. Optical-detection of ultrasound at a distance using a confocal Fabry-Perot-interferometer. *Appl. Phys. Lett*. 47(1):14–16.
49. Hamilton, J.D., and M.O'Donnell. 1998. High frequency ultrasound imaging with optical arrays. *IEEE Trans. Ultrason. Ferroelectr. Freq. Control* 45(1):216–35.
50. Sakadžić, S., and L.H.V. Wang. 2004. High-resolution ultrasound-modulated optical tomography in biological tissues. *Opt. Lett.* 29(23):2770–72.
51. Massie, N.A., M. Dunn, D. Swain, S. Muenter, and J. Morris. 1983. Measuring laser flow-fields with a 64-channel heterodyne interferometer. *Appl. Opt.* 22(14):2141–51.
52. Chan, K.P., K. Satori, and H. Inaba. 1998. Laser imaging through scattering media by enhanced heterodyne detection and speckle averaging using 2D detector array. *Electron. Lett*. 34(11):1101–103.
53. Nakata, T., and T. Ninomiya. 2004. Practical realization of high-speed photodisplacement imaging by use of parallel excitation and parallel heterodyne detection: A numerical study. *Appl. Opt.* 43(16):3287–96.
54. Nakata, T., and T. Ninomiya. 2005. Simultaneous real-time imaging of surface and subsurface structures from a single space-frequency multiplexed photodisplacement interferogram. *Appl. Opt.* 44(27):5809–17.
55. Nakata, T., K. Yoshimura, and T. Ninomiya. 2006. Real-time photodisplacement microscope for high-sensitivity simultaneous surface and subsurface inspection. *Appl. Opt.* 45(12):2643–55.

56. Lamont, M., and P. C. Beard. 2006. 2D imaging of ultrasound fields using CCD array to map output of Fabry-Perot polymer film sensor. *Electron. Lett*. 42(3):187–89.
57. Köstli, K.P., M. Frenz, H.P. Weber, G. Paltauf, and H. Schmidt-Kloiber. 2001. Optoacoustic tomography: Time-gated measurement of pressure distributions and image reconstruction. *Appl. Opt.* 40(22):3800–9.
58. Köstli, K.P., D. Frauchiger, J.J. Niederhauser, G. Paltauf, H.P. Weber, and M. Frenz. 2001. Optoacoustic imaging using a three-dimensional reconstruction algorithm. *IEEE J. Select. Top. Quantum Electron.* 7(6):918–23.